Chemical Geology 583 (2021) 120453

Contents lists available at ScienceDirect

Chemical Geology

journal homepage: www.elsevier.com/locate/chemgeo

Effects of structural cobalt on the stability and reactivity of hausmannite and manganite: Cobalt coordination chemistry and arsenite oxidation

Boyoung Song [a], Elizabeth B. Cerkez [b], Evert J. Elzinga [c], Bojeong Kim [a,*]

[a] Department of Earth and Environmental Science, Temple University, Philadelphia, PA 19122, United States
[b] Department of Chemistry, Temple University, Philadelphia, PA 19122, United States
[c] Department of Earth and Environmental Sciences, Rutgers University, Newark, NJ 07102, United States

ARTICLE INFO

Editor: K Johannesson

Keywords:
Hausmannite
Manganite
Cobalt
Arsenic
XAS
ATR-FTIR

ABSTRACT

Hausmannite and manganite, the most abundant Mn(II/III) oxides in the environment, commonly contain cobalt (Co) as a structural impurity, yet the effects of Co substitution on the structure, stability, and reactivity of Mn(II/III) oxides have not been experimentally assessed. Using pristine and Co-substituted minerals with varying Co loadings (1 and 2 wt%), the present study observed changes in the structural properties, as well as stability and reactivity of these minerals toward acidic and reductive dissolution with arsenite (As(III)). Cobalt substitution in hausmannite produced significant changes in the lattice parameters and surface areas of the mineral, while manganite presented little to no Co substitution effects. In both minerals, Mn and Co release was accelerated in reductive dissolution, although more than 85% of the Co remained in the mineral structure. Only hausmannite showed increased oxidation of As(III) to As(V) with increased Co substitution, where the stoichiometric $[Mn(II)]_{aq}$ to $[As(V)]_{aq}$ ratio was at/close to 2. X-ray absorption spectroscopy analysis indicated the co-presence of Co(II) and Co(III) at tetrahedral and octahedral sites, respectively, with structural Co(II) dominating in hausmannite. The sole occupancy of Co(II) at octahedral sites in manganite appeared to induce changes in the average Mn oxidation state. Multiple surface complexes of arsenate were observed on the mineral surfaces, with the bidentate binuclear mode being the major species. Thus, Co substitution altered the stability and reactivity of the Mn(II/III) oxides under dissolution conditions, although the extent varied by the Co coordination chemistry, valence, and quantity in the mineral structures.

1. Introduction

The occurrence and geochemical behavior of cobalt (Co) at Earth's surface is closely associated with that of manganese (Mn) (oxyhydr) oxides (hereafter, Mn oxides). The intimate association of Mn—Co has been extensively observed in soils (Burns, 1976; Koschinsky and Halbach, 1995; Manceau et al., 1987; Taylor, 1968; Taylor et al., 1964; Taylor and McKenzie, 1966), lake sediments (Green et al., 2004; Shacat et al., 2004), oceanic nodules (Burns et al., 1977; Dillard et al., 1982; Goldberg, 1954; Hein and Koschinsky, 2014; Koschinsky and Halbach, 1995), and ore deposits (Carpenter et al., 1978; Hem et al., 1989; Hem and Lind, 1994; Kay and Conklin, 2001; Ostwald, 1984; Tan et al., 2010), and such field observations have motivated laboratory-scale mechanistic studies aimed at understanding Co adsorption, oxidation, and structural incorporation by Mn oxides (Lee and Tebo, 1994; Manceau et al., 1997, 1992; McKenzie, 1972; Silvester and Manceau, 1997; Simanova and Peña, 2015; Wu et al., 2019; Yin et al., 2014, 2011; Yu et al., 2012). In particular, birnessite group minerals, the most common natural Mn(III/IV) oxides, have been extensively analyzed. In layered birnessite minerals adsorption of Co(II) occurs preferentially at edge sites and then migrates into vacant sites (Manceau et al., 1997; Simanova and Peña, 2015; Yin et al., 2011). Oxidation of adsorbed Co(II) to Co(III) can be facilitated by either Mn(IV) or Mn(III) (Crowther et al., 1983; Dillard et al., 1982; Hem, 1978; Manceau et al., 1997; Murray et al., 1985; Murray and Dillard, 1979; Simanova and Peña, 2015; Yin et al., 2011) or by O_2 in the presence of Mn(III/IV) minerals (Hem, 1978; Murray et al., 1985; Murray and Dillard, 1979), which is followed by incorporation of Co(III) into mineral structures (Crowther et al., 1983; Manceau et al., 1997, 1992; Simanova and Peña, 2015; Yin et al., 2011).

While the mechanisms of Co uptake and sequestration are well established in birnessite structure, only a few studies have investigated the effects of structurally incorporated Co on the stability and reactivity

* Corresponding author.
E-mail address: bkim@temple.edu (B. Kim).

https://doi.org/10.1016/j.chemgeo.2021.120453
Received 18 May 2021; Received in revised form 14 July 2021; Accepted 21 July 2021
Available online 27 July 2021

of Mn minerals, as well as the fate and cycling of the structural Co during geochemical processes. For instance, Yin et al. (2011) demonstrated that Co substitution in the hexagonal birnessite structure increased the removal capacity of Pb(II) and As(III) by the mineral, but produced insignificant Co and Mn in solution, implying that both metal cations were retained in the layered structure of birnessite, or strongly adsorbed onto the mineral surfaces. Furthermore, a recent study by Wu et al. (2019) demonstrated that Co remained incorporated in the crystal structures, and distributed among mineral mixtures, when Co-containing birnessite precursors underwent transformation processes. Thus, Co substitution in birnessite appears to enhance the overall reactivity of the minerals and Co tends to remain associated with the mineral lattice, either adsorbed or incorporated, during these reactions.

In addition to the birnessite family, naturally-occurring Mn(III)-oxide phases, such as hausmannite ($Mn(II)Mn(III)_2O_4$) and manganite (Mn(III)O(OH)), commonly contain Co as a structural impurity. Field-scale studies noted a correlation between an increase in reductive dissolution of hausmannite to an increase in Co solubility in lake and sedimentary environments (Green et al., 2004; Shacat et al., 2004). However, due to the complexity of redox boundaries in such environments, linking the Mn reduction solely to the geochemical behavior of Co was difficult to discern. In laboratory-scale studies, pristine phases of hausmannite and manganite have been favorably used for adsorption and redox reactions with heavy metals (including Co) and toxic metalloids (Chiu and Hering, 2000; Hem, 1978; Junta and Hochella, 1994; McKenzie, 1972; Shaughnessy et al., 2003; Song et al., 2021, 2020; Vodyanitskii, 2009; Weaver et al., 2002; Weaver and Hochella, 2003; Wilk et al., 2005). Research has also demonstrated that adsorption of Co (II) and oxidation of adsorbed Co(II) to Co(III) occurs on the surfaces of hausmannite or manganite, followed by structural incorporation of Co (III) (Hem, 1978; Simanova and Peña, 2015; Wu et al., 2019), similar to Co uptake by birnessite minerals. Yet, no studies exist which investigates influences in the characteristics and reactivity of these Mn(II/III) oxides induced by Co substitution, or the fate of structural Co as the minerals undergo geochemical reactions. A recent study of our own demonstrated that trace-level substitution of Ni in the hausmannite structure significantly altered the stability and reactivity of the mineral compared to the pristine phase (Song et al., 2020). As Ni is redox inactive under environmental conditions, the potential contribution of redox-labile Co to the oxidizing ability of the mineral is thus of particular interest.

In the present study, we characterized for the first time the similarities and differences of Co oxidation states and coordination chemistry in the structures of Co-substituted hausmannite and manganite, and demonstrated how these effects govern the properties, stability, and overall reactivity of the minerals toward acidity and/or arsenite (As(III)) relative to the pristine equivalents using a combination of laboratory and synchrotron-based techniques. The findings of the present study will help elucidate the complexity of intimate Mn—Co association in Mn(II/III) oxides, and thus improve our understanding of the stability or solubility of Mn oxides, as well as the fate and cycling of associated transition metals and metalloids in surficial environments.

2. Materials and methods

2.1. Materials

All chemical agents used for material synthesis and batch experiments in the present study were of analytical grade or better, including manganese acetate tetrahydrate ($Mn(CH_3COO)_2{\cdot}4H_2O$), cobalt acetate tetrahydrate ($Co(CH_3COO)_2{\cdot}4H_2O$), cobalt chloride hexahydrate ($CoCl_2{\cdot}6H_2O$), potassium persulfate ($K_2S_2O_8$), sodium (meta)arsenite ($NaAsO_2$), sodium arsenate dibasic heptahydrate (H_2NaAsO_4), acetone (CH_3COOH), ethyl alcohol (C_2H_5OH), sodium chloride (NaCl), nitric acid (HNO_3), hydrochloric acid (HCl), and sodium hydroxide (NaOH). Trace metal grade Mn, Co, and As standard solutions were used for inductively coupled plasma optical emission spectroscopy (ICP-OES) analysis. Dionex™ AS22 eluent consisted of 4.5 mM sodium carbonate and 1.4 mM sodium bicarbonate. Detailed information (e.g., manufacturer, purity) about chemicals can be found Supporting Information (SI), S1.1.

2.2. Material synthesis

Both pristine hausmannite (Song et al., 2020; Song et al., 2012) and manganite (Hu et al., 2008; Song et al., 2021) were synthesized following a method described in previous studies. The Co-substituted hausmannite was synthesized in the same manner as pristine hausmannite but with the addition of Co from a stock solution of 50 mM Co ($(CH_3COO)_2{\cdot}4H_2O$) into the $Mn(CH_3COO)_2{\cdot}4H_2O$ solution to meet the target 1 or 2 weight percent (wt%). Hereafter, these synthesized hausmannite minerals are referred to as Haus, Co1-Haus, and Co2-Haus, respectively. The Co-substituted manganite was synthesized in the same manner, by adding a stock solution of $Co(CH_3COO)_2{\cdot}4H_2O$ into the dissolved $Mn(CH_3COO)_2{\cdot}4H_2O$ solution to yield 1 or 2 wt%, respectively. Hereafter, these are referred to as Mang, Co1-Mang, and Co2-Mang, respectively. In contrast, mineral samples of Co adsorbed hausmannite or manganite was prepared by adding 1 mM of Co(II) (from 50 mM $CoCl_2{\cdot}6H_2O$ stock solution) into a suspension of pristine hausmannite or manganite (particle loading of 1 g/L). The adsorption reaction was continued for 24 hours (h) with solution pH maintained at pH 5 using dilute NaOH. After completion of the synthesis or adsorption reaction, the minerals were collected by centrifugation, rinsed several times with DI water, and then dried in an oven at 60 °C overnight prior to PXRD measurements.

2.3. Material characterization

Freshly-synthesized hausmannite and manganite minerals were characterized for structure, surface area, as well as elemental composition, by using a series of techniques including powder X-ray diffraction (PXRD) analysis, Brunauer-Emmett-Teller (BET) method, ICP-OES, and scanning electron microscopy (SEM), prior to batch reactions.

2.3.1. PXRD analysis

Powder mineral samples were analyzed by PXRD using a D8 Advance X-ray diffractometer (Bruker, USA) equipped with Ni-filtered, Cu *Kα* radiation, and a high-speed energy-dispersive linear detector (LYNXEYE). Sample powders were deposited on a non-diffracted silicon (Si) sample holder and scanned from 10 to 80° 2θ with a 0.01° step-size. Peak identifications were made using the DIFFRAC.EVA software with the American Mineralogy Crystal Structure Database (AMCSD). The lattice parameters of the unit cells were estimated with Rietveld refinement using total pattern analysis solution (TOPAS) software.

2.3.2. BET surface area analysis

The BET method was used to analyze approximately 100 mg of mineral sample with nitrogen gas (N_2) adsorption and desorption isotherm via a Quantachrome Monosorb surface area analyzer. The standard calibration was made using 1 cm^3 of air injected through a gas-tight glass syringe equipped with a cemented needle (C series, Pressure lok® analytical syringe, Valco Instruments Co. Inc). All surface area (SA) measurements were run in triplicate and used to calculate the average and standard deviation of SA for each mineral sample.

2.3.3. Elemental analysis

Both Co-substituted hausmannite and manganite samples were analyzed by two different approaches for elemental composition. First, a microwave-assisted acid digestion method (U.S. EPA, 2007) followed by ICP-OES analysis (iCAP 7400 equipped with Cetax autosampler) was employed to determine the total Mn and Co concentrations in the mineral samples. Approximately 20–30 mg of mineral sample were pre-digested with 10 mL of concentrated HNO_3 at room temperature

overnight, followed by microwave-assisted digestion at 200 °C for 20 minutes (min) using MARS 6 (CEM Corp.). The acid digests were collected and diluted with DI prior to ICP-OES, and analyzed with radial viewing for Mn (257.610 nm), while axial viewing was used for Co (228.616 nm) to increase sensitivity for trace metal detection.

A Quanta™ 450 FEG SEM equipped with Bruker QUANTAX 400 energy dispersive X-ray spectrometer (EDX) was also used to quantify the total Mn and Co contents in the mineral samples. Approximately 10 mg of mineral sample were sonicated in 30 mL of DI water by a probe sonicator (Model 505 Sonic Dismembrator, Fisher Scientific™) for 10 seconds (s). About 20–50 μL of the dispersed mineral suspension was placed on a Si wafer (University Wafer, Inc.) and dried at room temperature prior to the SEM analysis.

2.4. Batch experiments and solution analyses

Batch experiments with pristine or Co-substituted minerals were carried out at pH 5 in the absence (i.e., acidic dissolution) or presence (i.e., reductive dissolution) of As(III) ($NaAsO_2$) via established methodology described from prior work (Song et al., 2021, 2020). In brief, a mineral suspension was made by dispersing 30 mg of pristine or Co-substituted hausmannite in 149.25 mL of 10 mM NaCl solution by a probe sonicator, or the same particle loading of pristine or Co-substituted manganite prepared in 149.85 mL of 10 mM NaCl solution. For acidic dissolution reactions, the mineral suspension was titrated to pH 5.0 using dilute HCl or NaOH and equilibrated for one hour prior to use in batch reactions. For reductive dissolution reactions, the mineral suspension was prepared in the same fashion as the acidic dissolution, but 750 μL of a 50 mM $NaAsO_2$ stock solution was added into the hausmannite mineral suspension for a final concentration of 250 μM of As(III). Based on our recent study (Song et al., 2021) and a work by Chiu and Hering, (2000), a lower As(III) concentration of 50 μM was used for pristine and Co-substituted manganite minerals for the reductive dissolution reactions by adding 150 μL of a 50 mM $NaAsO_2$ stock solution.

Both acidic and reductive dissolution reactions were run for 8 h in duplicate with adjustments by dilute HCl to pH 5.0 as needed. A total of 11 aliquots were withdrawn from each replicate at selected times during the reaction, filtered with a 0.22 μm syringe filter (Millipore filter), and acidified with HNO_3. The acidified aliquots were then analyzed for total dissolved concentration of Mn, Co, and As by ICP-OES, where Mn and Co detected as described above (Section 2.3.3) and As detection was completed in axial view at 189.042 nm. In addition, As(V) concentrations were measured by ion chromatography (IC, Dionex™, ICS-1000, Thermo Scientific), equipped with a Dionex IonPacAS22 analytical column (4 mm × 250 mm) and a conductivity detector. At the end of each batch reaction, the reacted solids were collected by centrifugation, rinsed thoroughly with DI water, dried, and stored in a glove bag (Erlab 2200ANM, Erlab™) under N_2 prior to post-reaction analysis.

2.5. XAS analysis

X-ray absorption spectroscopy (XAS) data were collected at the Co, Mn, and As *K*-edges at two beamlines of the National Synchrotron Light Source II (NSLS II), Brookhaven National Laboratory (Upton, NY). The Co and Mn *K*-edge spectra were collected at beamline 6-BM, after beamline calibration with Co or Mn foil for the absorption edge location and the reference energy level (I_r). The Co *K*-edge spectra were collected at room temperature in fluorescence mode, whereas Mn *K*-edge spectra in transmission mode. The As *K*-edge spectra were collected at the Quick X-ray Absorption and Scattering (QAS) beamline (7-BM) to avoid As oxidation during XAS measurements (Nesbitt et al., 1998). The beamline was calibrated with Pt foil, and the As *K*-edge spectra were collected during 5 min at room temperature in fluorescent mode, with each scan requiring only 30 s.

For Co speciation, CoO (US Research Nanomaterials, Inc.), Co_3O_4, and CoOOH were used as reference materials and run under the same sampling conditions. For Mn speciation, birnessite (MnO_2) (McKenzie, 1971), manganite (MnOOH) (Hu et al., 2008; Song et al., 2021), and hausmannite (Mn_3O_4) (Song et al., 2020; Song et al., 2012) were synthesized in the laboratory via methods described in previous studies, and used as reference materials for XAS analysis. For As speciation, $NaAsO_2$, Na_2HAsO_4, and As(V)-reacted minerals were used as reference materials. Details on synthesis of the Co reference materials and preparation of As (V)-reacted minerals can be found in SI, S1.2.

The X-ray absorption spectra were analyzed both in the X-ray absorption near-edge structure (XANES) and extended X-ray absorption fine structure (EXAFS) energy regions. The XANES spectra for Co, Mn, and As were background-corrected, averaged, and normalized using the Athena graphical user interface (Ravel and Newville, 2005). Linear combination fitting (LCF) of the relevant XANES regions for Co was conducted from −20 to 20 e*V* of E°. The EXAFS spectra for Co and As were processed using the Artemis software, with k^3 weighting in the approximate range from about 3.0 to 9.0 $Å^{-1}$ for Co *K*-edge and As *K*-edge, and 3.0 to 12.0 $Å^{-1}$ for Mn *K*-edge (Ravel and Newville, 2005). During the EXAFS spectra fitting analysis, the coordination number (N) was fixed, while the rest of parameters, including E°, Debye-Waller factor (σ^2), and radial distance (R), were allowed to vary. Crystallographic information files for the reference materials were obtained from AMCSD and run with ATOMS and FEFF for calculation of the theoretical scattering pathways used in the fitting procedure.

2.6. Flow-cell ATR-FTIR

The attenuated total reflection Fourier transform infrared spectroscopy (ATR-FTIR) measurements were performed on hausmannite mineral surfaces (Haus, Co1-Haus and Co2-Haus) with As(III) ($NaAsO_2$) using a Smart Orbit ATR diamond accessory housed in a Nicolet 6700 spectrometer (Thermo Scientific™) equipped with a liquid N_2-cooled MCTA detector, following established methodology described in our prior work (Bhandari et al., 2010; Cerkez et al., 2015; Song et al., 2020). In brief, ~75 to 100 μL of a mineral suspension (~ 0.08 mg of mineral in the suspension) was deposited on the ATR element, and dried under N_2. Then, a house-made Teflon flow cell was placed around the mineral film, followed by equilibration with 10 mM NaCl solution at pH 5. Once the film was equilibrated (confirmed by constant spectra), a solution of 250 μM As(III) (or As(V)) (in 10 mM NaCl at pH 5) was introduced to the film for 2 h at a flow rate of 1 mL/min. Spectra were collected from 650 to 4000 cm^{-1} at a resolution of 4 cm^{-1}, resulting in 200 co-added scans for each time point. All spectra were processed by blank and background subtraction. It is noted that due to low As(III) (or As(V)) interaction on manganite mineral surfaces, no ATR-FTIR measurements were made on manganite samples.

3. Results and discussion

3.1. Effects of Co substitution in the Mn(II/III) oxide structures and properties

The effects of Co substitution in the structures and properties of lower valence Mn oxides were examined by comparing Co-substituted Haus or Mang to pristine equivalents for crystallographic properties, particle size, and surface area (SA). The importance of these properties on mineral dissolution reactions has been also noted in our recent work (Song et al., 2020), as well as other studies (Eitel et al., 2018; Luo et al., 2018; Peña et al., 2007). Prior to a series of comparison, the quantification of Co and Mn in Co-substituted Haus or Mang was made to ensure the target wt% of Co to Mn in each mineral sample. The results of the ICP-OES analysis on Co1-Haus and Co2-Haus showed 1.0 and 2.8 wt% of Co (and hence, 99.0 and 97.2 wt% of Mn), respectively, and 1.0 and 2.6 wt% of Co (99.0 and 97.4 wt% of Mn) in Co1-Mang and Co2-Mang, respectively. In addition, the SEM EDX results displayed Co wt% of

0.7 and 2.0 for Co1-Haus and Co2-Haus (Table S1 and Fig. S1), respectively, and of 1.4 and 3.5 for Co1-Mang and Co2-Mang (Table S2 and Fig. S2), respectively. Both techniques resulted in values that were in good agreement for the quantification of Co and Mn in Co-substituted minerals.

The PXRD patterns of Co1-Haus and Co2-Haus were well-matched to that of pristine Haus and the reference material (hausmannite, AMCSD 0002024) (Fig. 1(a)) and formation of Co (hydr)oxides or other mineral phases was not observed. Co substitution in the hausmannite structure caused peak sharpening and slight peak shifting toward higher 2θ, more distinguishable with increasing Co substitution (Fig. 1(a)). By analyzing unit cell parameters derived from Rietveld refinement (Table S3), the unit cell lattice parameter along the *c*-axis decreased from 9.4522 to 9.4093 Å, as Co substitution increased in the hausmannite structure, while the other parameters remained relatively consistent. The contraction in *c*-axis is attributed to changes in the lattice size induced by the replacement of a larger Mn cation with a smaller Co in the structure (Shannon, 1976). Such changes in lattice parameters have been noted elsewhere (Wright et al., 1992; Yamamoto et al., 1983), and also with Ni substitution in the hausmannite structure (Song et al., 2020). In contrast to hausmannite, the PXRD patterns of Co1-Mang and Co2-Mang were identical to that of pristine Mang and the reference material (manganite, AMCSD 0010565) (Fig. 1(b)), showing no changes in the PXRD patterns and subsequent derived unit cell parameters. This is presumably due to compatible metal ion sizes for substitution in the mineral structure, such as a high-spin (HS) Mn(III) with low-spin (LS) of Co(II) (Table S4).

To further confirm that Co was structurally incorporated in hausmannite and manganite, not adsorbed on those mineral surfaces, PXRD patterns of Co-adsorbed Haus and Mang were collected and compared with those of the pristine equivalents. The PXRD patterns of Co-adsorbed Haus were identical to those of pristine hausmannite and the reference, without signs of peak sharpening and shifting (Fig. S3(a)), both of which were evident in the PXRD patterns of Co-substituted Haus. The PXRD patterns of Co-adsorbed manganite were also identical to those of the pristine and reference minerals, except that an additional peak was observed in Co-adsorbed Mang which was not seen in the PXRD patterns of pristine or Co-substituted manganite (Fig. S3(b), indicated by box). This additional feature may indicate the presence of an impurity by added Co, as no match was found with DIFFRAC.EVA software or with the AMCSD. The absence of this feature in both pristine and Co-substituted Mang minerals supports Co substitution in the manganite structure, not Co adsorption on the mineral surfaces.

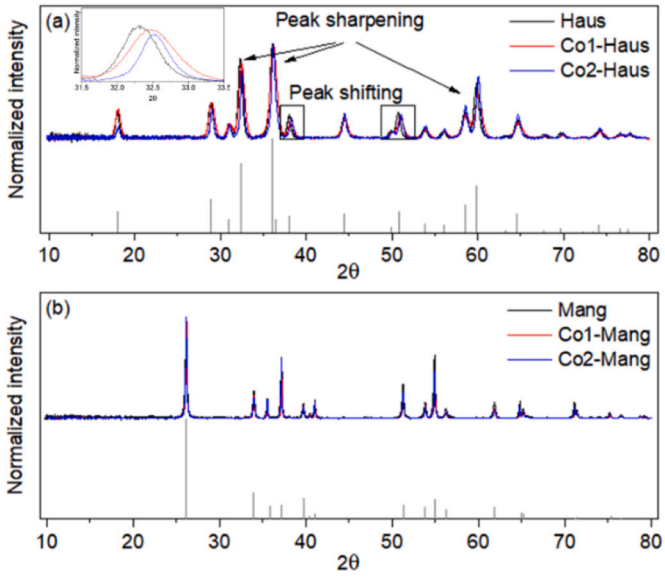

Fig. 1. Full PXRD spectra of (a) Haus (black), Co1-Haus (red), and Co2-Haus (blue), with the hausmannite reference (AMCSD 0002024). An inset of enlarged diffractogram as an example shows a shift to higher 2θ with increasing Co substitution and (b) Mang (black), Co1-Mang (red), and Co2-Mang (blue) with the manganite reference (AMCSD 0010565). (For interpretation of the references to colour in this figure legend, the reader is referred to the web version of this article.)

The results of BET SA analysis also showed the effect of Co substitution in hausmannite and manganite, where the Co-substituted minerals had lower SA compared to the pristine phases (Table S3). Pristine Haus had the highest BET SA of 136 (±1) m^2/g, followed by Co1-Haus and Co2-Haus, 112 (±1) and 100 (±2) m^2/g, respectively. A 26.5% decrease in the BET SA from pristine Haus was made by 2 wt% Co substitution in the mineral structure. Similarly, pristine Mang had the highest BET SA of 28.5 (±0.4) m^2/g, followed by Co1-Mang and Co2-Mang, 27.1 (±0.5) and 26.3 (±0.2) m^2/g, respectively, a 7.7% decrease from pristine Mang caused by 2 wt% Co substitution. The decreases in BET SA by Co substitution may be attributed to increases in crystal size with increasing levels of Co substitution. Such changes in SA by Co substitution have been observed in MnO_2-type minerals (Wu et al., 2019), and also by Ni substitution in hausmannite samples (Song et al., 2020).

3.2. *Effects of Co substitution on the Mn(II/III) oxide dissolution reactions*

3.2.1. *Acidic dissolution of pristine and Co-substituted Mn(II/III) oxides*

The effect of Co substitution on the reactivity and stability of low valence Mn oxides was evaluated by measuring the extent of Mn and/or Co release as a result of acidic mineral dissolution. At pH 5, all hausmannite samples readily underwent dissolution, releasing Mn(II) into solution (Table S5). After 8 h of the acidic dissolution reaction, Haus, Co1-Haus, and Co2-Haus produced 130 (±1), 139 (±5), and 158 (±3) μM $[Mn(II)]_{aq}$, respectively, where Co2-Haus recorded the highest $[Mn(II)]_{aq}$ release despite the lowest BET SA. When released $[Mn(II)]_{aq}$ was further normalized by SA, the values were at 4.8, 6.2, and 7.9 $\mu M \cdot m^{-2}$, for Haus, Co1-Haus, and Co2-Haus, emphasizing the enhanced dissolution of hausmannite with higher Co substitution (Detail calculation is in SI S3.1). This finding implies that the structural incorporation of Co in hausmannite accelerates acidic mineral dissolution, more significantly at 2 wt% than 1 wt% substitution. A similar observation was made with Ni substitution in hausmannite, where a higher $[Mn(II)]_{aq}$ was measured from Ni-substituted hausmannite than the pristine at pH 5 (Song et al., 2020). In addition, the concomitant release of structural Co was also noted, 0.2 (±0.1) and 1.3 (±0.1) μM $[Co(II)]_{aq}$ in Co1-Haus and Co2-Haus, respectively. When considering the fraction of $[Co(II)]_{aq}$ of the total metal released (i.e., $[Mn(II)]_{aq} + [Co(II)]_{aq}$) for Co1-Haus and Co2-Haus, the percentage attributed to Co was 0.1 and 0.8%, respectively, values lower than the wt% of Co in the mineral structures. Thus, the overall release of structural Co from both Co1-Haus and Co2-Haus was minimal, with the majority of Co remaining in the hausmannite structures after 8-h acidic dissolution. Details of this calculation are provided in SI S3.2.

In contrast to hausmannite, limited acidic dissolution was observed in manganite minerals. The release of structural Mn was only observed in Co-substituted manganite but not in pristine, with measured $[Mn(II)]_{aq}$ of 2.3 (±1.4) and 4.9 (±0.9) μM observed from Co1-Mang and Co2-Mang, respectively. Normalization of Mn release by SA yielded values of 0.4 and 0.9 $\mu M \cdot m^{-2}$ for Co1-Mang and Co2-Mang, respectively, thus displaying a similar trend as the hausmannite system, where an increase in $[Mn(II)]_{aq}$ was observed with increased Co substitution (Detail calculation is in SI S3.1). The release of structural Co was not observed during acidic mineral dissolution of manganite samples (Table S5). The stability of manganite against acidic dissolution has been experimentally demonstrated in previous studies (Luo et al., 2017; Murray et al., 1985; Stumm and Giovanoli, 1976; Weaver et al., 2002). Despite the small quantities observed here, the results indicate that Co

substitution in the structure can make manganite more susceptible to acidic dissolution.

3.2.2. *Reductive dissolution of pristine and Co-substituted Mn(II/III) oxides by arsenite*

The effect of Co substitution on the reactivity and stability of low valence Mn oxides was also evaluated by measuring the extent of reductive mineral dissolution in the presence of As(III). Both hausmannite (Barreto et al., 2020; Silva et al., 2013; Song et al., 2020) and manganite (Chiu and Hering, 2000; Song et al., 2021) oxidize As(III) to As(V), releasing Mn(II) into the solution during As(III) oxidation. Hence, the quantity of As(V), Mn(II), and/or Co(II) (i.e., $[As(V)]_{aq}$, $[Mn(II)]_{aq}$ and/or $[Co(II)]_{aq}$) produced as a result of reductive dissolution were used as means of comparison between Co-substituted minerals and the pristine equivalents. Based on the above results, especially for $[Mn(II)]_{aq}$ and/or $[Co(II)]_{aq}$, both acidic and reductive dissolution reactions are assumed to contribute at pH 5. Thus, in order to estimate the extent of $[Mn(II)]_{aq}$ and/or $[Co(II)]_{aq}$ induced by the reductive dissolution only, initial concentrations of Mn and/or Co measured prior to sample exposure to As(III) were subtracted from the measured concentrations of these elements.

In the presence of hausmannite, a majority of added As(III) was oxidized to As(V), with increasing $[As(V)]_{aq}$ over the course of the experiment. After 8 h, the measured $[As(V)]_{aq}$ of Haus, Co1-Haus, and Co2-Haus were 194 (±10), 163 (±8), and 144 (±2) μM, respectively (Fig. 2(a), open triangle), where less As(V) was observed in the Co-substituted samples. However, when the SA of the minerals was used to normalize $[As(V)]_{aq}$, the Co-substituted Haus showed more As(V) produced per meter squared, specifically 8.9, 9.9, and 9.8 $\mu M \cdot m^{-2}$ Haus, Co1-Haus and Co2-Haus, respectively (Detailed calculation is in SI S3.3). In addition, a loss of total As from solution was observed in all hausmannite samples (Fig. 2(a), closed triangle). The initial concentration of As(III) was 250 μM, thus the loss of As via adsorption onto mineral phases was estimated to be 19.0, 22.6, and 20.4% for Haus, Co1-Haus, and Co2-Haus, respectively, showing that the majority of arsenic remained in solution as As(V), consistent with observations made by Yin et al. (2011) and Song et al. (2021, 2020). These findings also agree well with measurements of the point of zero charge (PZC) of hausmannite to be below pH 5. Hence, at pH 5 the hausmannite surface is slightly negatively charged and not favorable for As(V) adsorption reactions.

The concomitant release of $Mn(II)_{aq}$ was also noted from the hausmannite samples under reductive dissolution conditions. In the Haus, Co1-Haus, and Co2-Haus batch reactions 362 (±11), 356 (±9), and 388 (±2) μM $[Mn(II)]_{aq}$, respectively, was detected after 8 h of the reductive dissolution reaction (Fig. 2(b), square). These concentrations are 2.5–2.8 times higher than the Mn release measured as a result of the acidic dissolution reactions alone, indicating accelerated mineral dissolution in the presence of As(III). Furthermore, when the $[Mn(II)]_{aq}$ was normalized by the SA of each mineral (13.3, 16.1, and 19.4 $\mu M \cdot m^{-2}$ for Haus, Co1-Haus, and Co2-Haus, respectively) a similar trend as the acidic dissolution was observed, with enhanced Mn(II) release with higher Co substitution per meter squared of mineral (Detail calculation is in SI S3.3). During reductive dissolution, structural Co in hausmannite was also released, 1.4 (±0.1) and 10.7 (±0.3) μM from Co1-Haus and Co2-Haus, respectively (Fig. 2(b), circle in the enlarged graph). Further, the $[Co(II)]_{aq}$ fraction relative to the total metals released (i.e., $[Mn(II)]_{aq}$ + $[Co(II)]_{aq}$) was 0.4 and 2.7% for Co1-Haus and Co2-Haus, respectively (See S3.2). These values are in the range of the Co substitution in the hausmannite structure, suggesting the reductive dissolution process occurs more aggressively than acidic dissolution alone. Finally, mass balance calculations of Co indicates that 85–94% of initial Co remained in hausmannite structure after the As(III) oxidation, suggesting a strong retention of Co during reductive dissolution (Table S6).

In the presence of manganite, significantly lower concentrations of As(V) were measured compared to hausmannite, 5 (±1), 6 (±1), and 8 (±2) μM $[As(V)]_{aq}$ in Mang, Co1-Mang, and Co2-Mang, respectively (Fig. 3(a), open triangle). These quantities account for less than 20% of the initial As(III) added being oxidized to As(V), indicating poor As(III) oxidizing ability of manganite compared to hausmannite. When the measured $[As(V)]_{aq}$ was normalized by the SA of each mineral (2.3, 2.2, and 2.5 $\mu M \cdot m^{-2}$ for Mang, Co1-Mang, and Co2-Mang, respectively), it was evident that Co substitution in the manganite structure had little to no impact on the oxidizing ability of the mineral (Detailed calculation is in SI S3.3). The As loss through adsorption on manganite surfaces was also noted, specifically, 16.4, 11.3, and 10.3% of the initial As(III) added (50 μM) was estimated to be adsorbed on Mang, Co1-Mang, and Co2-Mang, respectively (Fig. 3(a), close triangle). Lower oxidation and adsorption of As by manganite can be explained by weak electrostatic interactions between As species and mineral surfaces. At pH 5, manganite is positively charged (Ramstedt et al., 2004), with little to no attraction to the neutral As(III) species. This initially unfavorable surface interaction seems to limit As(III) oxidation to As(V), and subsequently, lower As(V) adsorption on the mineral (Guo et al., 2015; Song et al., 2021).

The release of aqueous Mn was also observed from manganite during reductive dissolution. The $[Mn(II)]_{aq}$ was 17.1 (±0.9), 16.9 (±3.0), and 25.0 (±0.5) μM in Mang, Co1-Mang, and Co2-Mang, respectively, after 8 h (Fig. 3(b), square). These levels are approximately five times higher than the Mn release observed during acidic dissolution alone. The SA normalized $[Mn(II)]_{aq}$ productions were 3.0, 3.1, and 4.8 $\mu M \cdot m^{-2}$ from

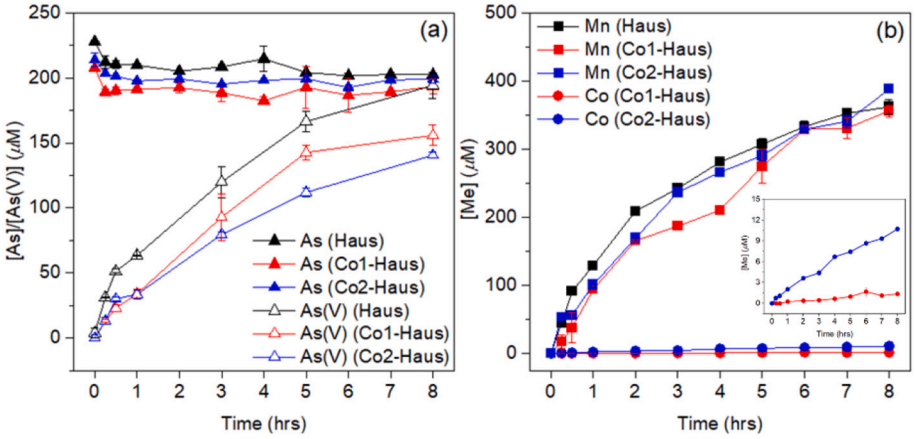

Fig. 2. The bulk solution analysis from arsenite oxidation by Haus (black), Co1-Haus (red), and Co2-Haus (blue). (a) $[As]_{tot}$ (closed triangle) and [As(V)] (open triangle), and (b) [Mn(II)] (closed square) and [Co(II)] (closed circle). An enlarged graph of $[Co(II)]_{aq}$ vs. time for better presentation. (For interpretation of the references to colour in this figure legend, the reader is referred to the web version of this article.)

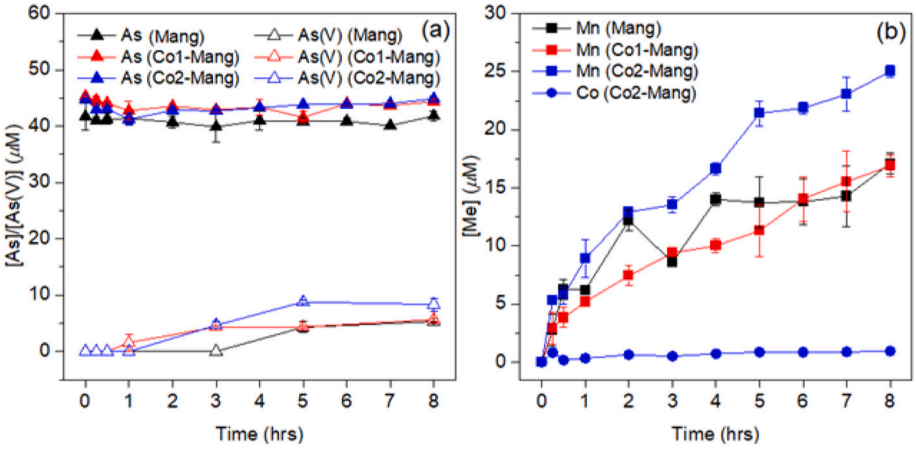

Fig. 3. The bulk solution analysis from arsenite oxidation by Mang (black), Co1-Mang (red), and Co2-Mang (blue). (a) $[As]_{tot}$ (closed triangle) and [As(V)] (open triangle) and (b) [Mn(II)] (closed square) and [Co(II)] (closed circle) as a function of time. (For interpretation of the references to colour in this figure legend, the reader is referred to the web version of this article.)

Mang, Co1-Mang, and Co2-Mang, respectively, also displaying an increase of Mn(II) release as Co substitution increased (Detailed calculation is in SI S3.3). The release of structural Co (1.0 (±0.1) μM $[Co(II)]_{aq}$) was detected only from Co2-Mang (Fig. 3(b), circle), representing 3.8% of total metal released, a percentage greater than the fraction measured in Co2-Haus (2.7%, See SI 3.2) and greater than the wt% in the mineral structure. However, the majority of Co remained in the manganite structure, similar to the strong Co retention observed in Co-substituted hausmannite samples (Table S6).

3.2.3. *Effects of Co substitution on Mn(II/III) oxide dissolution*

In order to generalize the effects of Co substitution on dissolution behaviors of Mn(II/III) oxides, the production of SA-normalized $[Mn(II)]_{aq}$ and the ratio of $[Mn(II)]_{aq}$ to $[As(V)]_{aq}$ were examined as a function of Co wt% in both minerals. First, when plotting the SA-normalized $[Mn(II)]_{aq}$ against the Co wt% of each mineral, four linear regressions were achieved, where an R^2 of 0.996 or higher for all samples was obtained, except for the reductive dissolution in manganite (R^2 of 0.797) (Fig. 4). Based on this analysis the extent of the mineral dissolution was increased by Co substitution in all Mn(II/III) oxides. Importantly, a ratio of the slopes shows a doubling of this effect when both reductive and acidic dissolution are operative rather than just acidic dissolution for both minerals. This may indicate there is a synergistic effect of the two dissolution reactions, where reductive dissolution actually enhances the rate of acidic dissolution.

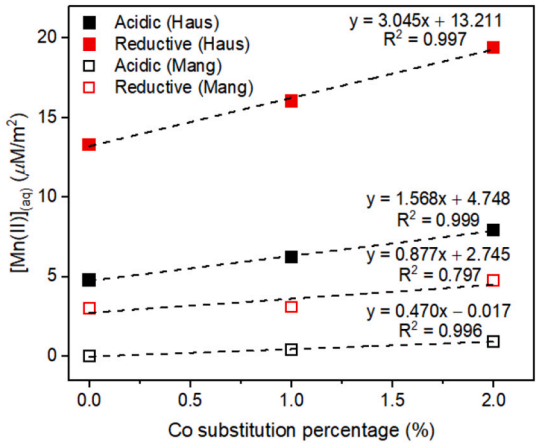

Fig. 4. The SA-normalized $[Mn(II)]_{(aq)}$ production derived from acidic (black) and reductive (red) dissolution of hausmannite (closed square) and manganite (open square) as a function of Co substitution percentage in the mineral structure. (For interpretation of the references to colour in this figure legend, the reader is referred to the web version of this article.)

Based on the stoichiometry of the As(III) oxidation reaction, with a theoretical ratio of 2 to 1 of $[Mn(II)]_{aq}$ to $[As(V)]_{aq}$ (Song et al., 2020, 2021), the ratios were calculated and compared between the pristine and Co-substituted phases in both minerals to probe the effects of Co substitution on the reductive dissolution. For Haus, Co1-Haus, and Co2-Haus these ratios were estimated to be 1.5:1, 1.7:1, and 2.0:1 after the 8-h reaction, respectively, while ratios of 1.3:1, 1.4:1, and 1.9:1 were determined for Mang, Co1-Mang, and Co2-Mang, respectively. While hausmannite minerals resulted in the ratios closer to the theoretical of 2, in both minerals higher Co wt% in substitution yielded ratios closer to 2, whereas the pristine phases recorded the lowest ratio of Mn(II):As(V). The results of these analyses show that the enhancement of mineral dissolution reactions occurs in the presence of structural impurity of Co, more significantly at higher substitution wt% in the structure.

3.3. *XAS of pristine and Co-substituted Mn(II/III) oxides before and after dissolution reactions*

Synchrotron based XANES and EXAFS analyses at the Co and Mn *K*-edges were used to assess differences in oxidation states and local coordination environments of these elements in the mineral solids before and after the dissolution reactions. Due to the low level of As sorption in the manganite systems, As *K*-edge XAS analysis was only feasible for hausmannite samples, and the results of As K-edge analysis are provided in SI, S4.1 (See Figs. S4, S5, and Table S7).

3.3.1. *Co K-edge XANES and EXAFS analysis: Co2-Haus*

The Co *K*-edge XANES data show that the spectrum of Co2-Haus is similar to $Co(II)Co(III)_2O_4$, in that the position of the absorption edge is located between those of the Co(II)O and Co(III)OOH references (Fig. 5 (a)). The similarity of the spectra of Co2-Haus and Co_3O_4 is attributed to the fact that both hausmannite and Co_3O_4 have normal spinel structures, with Mn(II) and Co(II) positioned in tetrahedral sites $(Mn(II)_{tet}$ and $Co(II)_{tet})$ and Mn(III) and Co(III) in octahedral sites $(Mn(III)_{oct}$ and $Co(III)_{oct})$ (Suchow, 1976), and thus, suggests that Co2-Haus contains Co in oxidation states of (II) and (III) in the mineral structure.

To further analyze the ratio between Co(II) and Co(III) in Co2-Haus, the first derivative of the pre-edge region of the normalized spectrum was compared to that of the Co_3O_4 reference material (Fig. 5(b)). Both Co_3O_4 and Co2-Haus present a peak at ~7717 eV, which corresponds to $Co(II)_{tet}$, and another at ~7721 eV, corresponding to $Co(III)_{oct}$ (Yildirim and Riesen, 2013). When analyzing the derivative spectrum of Co_3O_4,

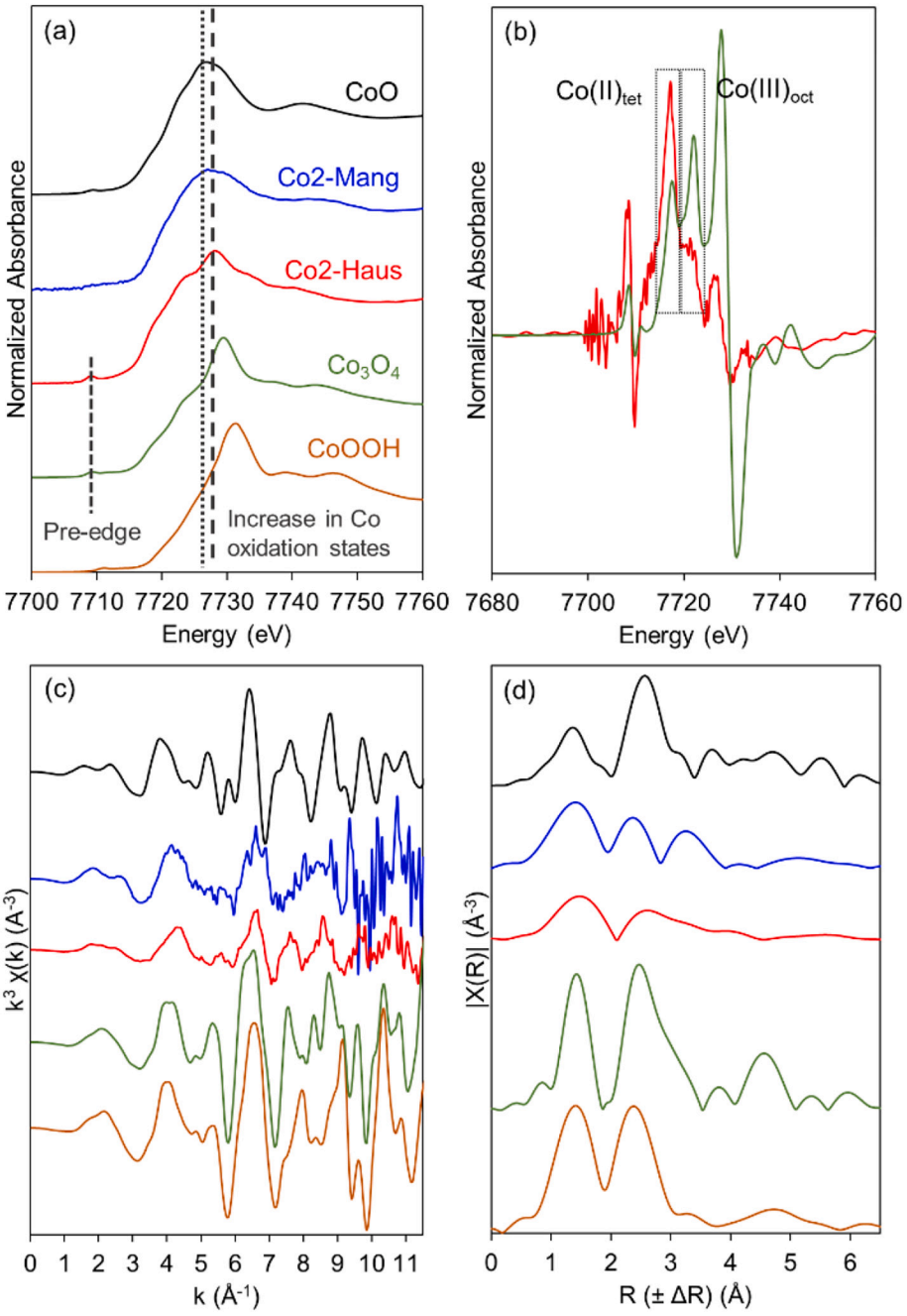

Fig. 5. Co *K*-edge X-ray absorption spectra of Co2-Haus (red) and Co2-Mang (blue) with reference materials, Co(II)O (black), $Co(II)Co(III)_2O_4$, (green), and Co(III)OOH (orange). (a) XANES regions marked with dashed lines at the absorbance edge locations showing different Co oxidation states among samples and reference materials, (b) Co2-Haus and Co_3O_4 reference in first derivatives, EXAFS regions in (c) k^3-weighted $\chi(k)$ function, and (d) the radial structure functions (RSFs). (For interpretation of the references to colour in this figure legend, the reader is referred to the web version of this article.)

the peak height ratio of Co(II) to Co(III) was 1 to 2 (Yildirim and Riesen, 2013), while a higher peak height of Co(II) relative to Co(III) in Co2-Haus was observed. This important difference indicated that the majority of Co in hausmannite is in the oxidation state of (II) and situated at the tetrahedral site, and only a minor quantity of Co exists as Co(III) at the octahedral site. Substitution of Co(II) at tetrahedral sites in the hausmannite structure has also been noted elsewhere (Miyasaka et al., 2012; Wright et al., 1992). The difference also provides further evidence that Co is incorporated into hausmannite structure rather than existing as a separate Co_3O_4 phase. In addition, we exclude the possibility of Co (II) oxidation to Co(III) during the XAS measurements, as no edge-shifts were observed during the triplicated measures of the Co-substituted samples, or during analysis of Co(II)-containing reference materials.

The average local coordination environments of cobalt in Co2-Haus were also examined by shell-by-shell fitting of the EXAFS spectra, via two single-scattering paths (—Co-O and Co-Me). The two spinel model compounds Co_3O_4 (having $Co(II)_{tet}$ and $Co(III)_{oct}$ at a 1:2 ratio) and $CoMn_2O_4$ (having $Co(II)_{tet}$ and $Mn(III)_{oct}$ at a 1:2 ratio) were used for the analysis. The best fits were obtained with Co—OCo-O ($N = 4$) and Co-Me ($N = 8$) at radial distances ($R_{Co\text{-}O}$ and $R_{Co\text{-}Me}$) of 1.96 and 3.39 Å, respectively (Fig. 6 and Table 1). While these $R_{Co\text{-}O}$ and $R_{Co\text{-}Me}$ values are comparable to Co(II) and Co(III) at tetrahedral and octahedral sites, respectively, in the hausmannite structure, they are located between those of the two model compounds, suggesting that the Co coordination environment in hausmannite is intermediate between these two materials (Table 1). The trend of $R_{Co\text{-}O}$ and $R_{Co\text{-}Me}$ values was observed in the order of $CoMn_2O_4$ > Co2-Haus > Co_3O_4, and such an increase of the —Co-O shell is related to a higher content of $Co(II)_{tet}$ than $Co(III)_{oct}$ in the hausmannite structure. The $R_{Co\text{-}O}$ value in Co_3O_4 compound is the shortest among all three compounds (1.92 Å, Table 1) due to the dominant presence of $Co(III)_{oct}$, which has a bonding distance of Co(III)-O of 1.89–1.91 Å (McKenzie, 1972; Wu et al., 2019). In addition, Co_3O_4

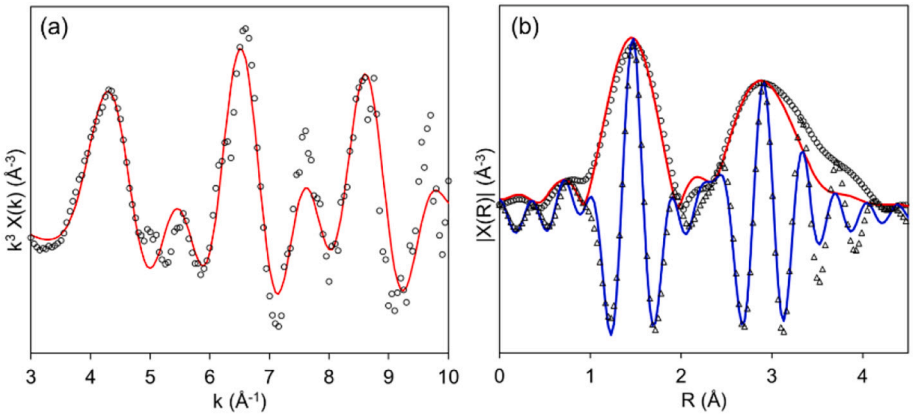

Fig. 6. Co *K*-edge EXAFS region of Co2-Haus: (a) k^3-weighted $\chi(k)$ function and (b) Fourier transforms (imaginary part in triangles, magnitude in circles) and their fitting results (solid line) corresponding to the Table 1.

Table 1
Co *K*-edge EXAFS spectra fitting parameters and results of Co2-Haus.

				Crystallographic values					
Co2-Haus				Co_3O_4[b]			$CoMn_2O_4$[c]		
Shell	N[a]	R (Å)	σ^2 (A^2)	Shell	N	R (Å)	Shell	N	R (Å)
O	4	1.96 (9)	0.002 (3)	O	4	1.92	O	4	2.02
Me	8	3.39 (5)	0.008 (3)	Co	12	3.35	Me	8	3.43

[a] N was fixed during the fitting analysis. R (radial distance) and its uncertainty is marked with ΔR. The σ^2 (A^2) is the Debye-Waller factor. All parameters are reported with estimated uncertainties for the fitting exercises (provided in the parentheses in the table), except fixed parameters.

does not exhibit the Jahn-Teller (JT) distortion with $Co(III)_{oct}$ in LS electron configuration (Wu et al., 2019), and hence, results in the shortest distance of Co-Me ($R_{Co\text{-}Me}$ 3.35 Å, Table 1).

While elongated $R_{Co\text{-}O}$ values were found in Co2-Haus and $CoMn_2O_4$ compared to Co_3O_4, the shorter $R_{Co\text{-}O}$ in Co2-Haus (1.96 Å) than in $CoMn_2O_4$ (2.02 Å) is evidence of cobalt residing in both tetrahedral and octahedral sites as Co(II) and Co(III) (Table 1), respectively, in hausmannite. Both the elongated $R_{Co\text{-}O}$ and higher ratio of $Co(II)_{tet}$ to $Co(III)_{oct}$ in Co2-Haus are also in good agreement with our own Co *K*-edge XANES analysis, as well as others (Miyasaka et al., 2012; Wright et al., 1992; Yamamoto et al., 1983). Furthermore, the presence of JT-distorted Mn(III) in Co2-Haus and $CoMn_2O_4$ can likely induce the elongation of $R_{Co\text{-}Me}$. The $R_{Co\text{-}Me}$ in Co2-Haus (3.39 Å, Table 1) was slightly shorter than that of $CoMn_2O_4$ (3.43 Å, Table 1), likely due to the minor quantity of $Co(III)_{oct}$ present in Co2-Haus. These structural variations are important for understanding the Co environment in hausmannite, where the relatively low occupation of Co(III) in LS electron configuration in octahedral sites may be explained by a lack of compatibility with the JT distorted trivalent site.

The Co *K*-edge EXAFS analyses indicate that the abundance of Co(II) relative to Co(III) increases in the sequence of Co_3O_4 < Co2-Haus < $CoMn_2O_4$. This implies substantial structural complexity in Co2-Haus, where two divalent metal ions (Mn(II) and Co(II)) and two trivalent metal ions (Mn(III) and Co(III)) coexist in both tetrahedral and octahedral coordinations, different from the relatively simple coordination chemistry of the model compounds. This mixed Co coordination in Co2-Haus is reflected not only in the XANES results (Fig. 5(a)), but also in the EXAFS spectra, where significant dampening in the oscillations of the χ spectra and in the peak height of the Fourier transforms are observed compared to the other materials (Fig. 5(c), (d)).

3.3.2. Co K-edge XANES and EXAFS analysis: Co2-Mang

The Co *K*-edge XANES spectrum of Co2-Mang was well-aligned with that of Co(II)O (Fig. 5(a)), suggesting Co(II) substitution at the octahedral sites in the manganite structure. The results of LCF analysis also support the sole presence of Co(II) in Co2-Mang sample (Data not shown). These findings are similar to a study by Hens et al. (2018), where divalent Ni substitution occurred at the octahedral sites of the manganite structure.

The EXAFS data of the Co2-Mang sample were fit in the same manner as Co2-Haus, using two scattering pathways (—Co-O and —Co-Me) and Co(III)OOH as the model compound (Fig. 7 and Table 2). The best fit for $R_{—Co\text{-}O}$ was found to be 1.94 Å, which is slightly longer than the reference (1.90 Å) and experimental (1.91 Å) values for heterogenite (Table 2) (Manceau et al., 1987; Wu et al., 2019). This increase in the —Co-O distance may be due to the larger Co(II) ions in manganite relative to smaller Co(III) in the model compound (Fig. 5(a)), and is suggestive of incorporation of Co in the mineral structure versus precipitation of a separate Co phase. The best fit for $R_{Co\text{-}Me}$ was found to be 2.87 Å, in strong agreement with the crystallographic values of the Co-Me distances reported in heterogenite (Table 2). The relatively high Debye-Waller factor (σ^2) fitted for this shell may reflect structural disorder arising from the substitution of octahedral Co(II) as an impurity in Mn (III) sites of the manganite structure.

3.3.3. Mechanism of structural Co incorporation in Mn(II/III) oxides

The results of the XAS analyses demonstrate for the first time the structural complexity in both hausmannite and manganite minerals induced by Co substitution. These experimental findings are supported by a theoretical analysis of crystal field stabilization energy (CFSE) values and bonding distances (Fig. 8(a)) (McKenzie, 1972). For example, in the hausmannite structure, only LS Co(III) (45 kcal/mol) possesses enough energy to replace Mn(III) (35.9 kcal/mol) at octahedral sites (McKenzie, 1972; Yin et al., 2011). Similarly, the replacement of Co(II) (12 kcal/mol) with a tetrahedral Mn(II) site (0 kcal/mol) is also energetically favorable (McClure, 1957), and the bonding distance of Mn(II)-O (2.04 Å) is comparable with that of Co(II)-O (2.02 Å). While energetically favorable in substitution, Co(III) in an LS electron configuration does not exhibit the JT distortion, as shown in Fig. 8(b). In contrast, HS Co(III) does display JT distortion, and therefore, this electron configuration would be more compatible when replacing HS Mn(III) in the hausmannite structure. Thus, substitution of LS Co(III) for HS Mn (III) may lower the stability of the hausmannite structure, making it more susceptible toward acidic and reductive mineral dissolution, results observed in Co-substituted Haus samples. This incompatibility of either HS or LS Co(III) substitution at Mn(III) octahedral sites may further explain the higher percentage of overall Co substitution in the hausmannite occurring at Mn(II) octahedral sites by Co(II).

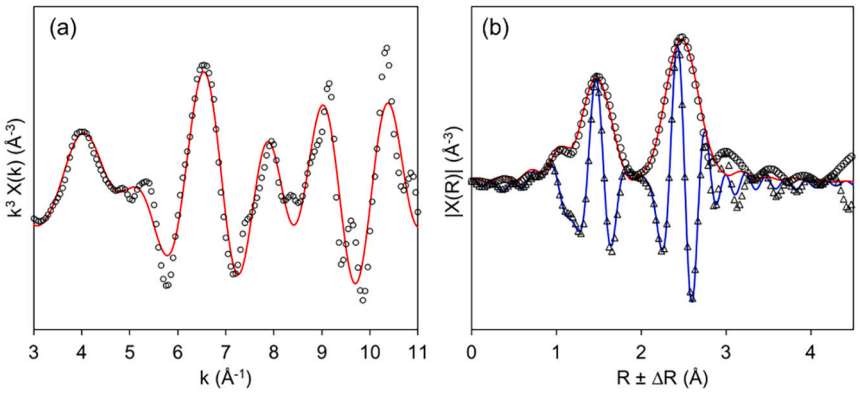

Fig. 7. Co *K*-edge EXAFS region of Co2-Mang: (a) k^3-weighted χ(k) function and (b) Fourier transforms (imaginary part in triangles, magnitude in circles) and their fitting results (solid line) corresponding to the Table 2.

Table 2
Co *K*-edge EXAFS spectra fitting parameters and results of Co2-Mang.

								Crystallographic values		
Co2-Mang				Co(III)OOH reference				Heterogenite[b]		
Shell	N[a]	R (Å)	σ^2 (A^2)	Shell	N	R (Å)	σ^2 (A^2)	Shell	N	R (Å)
O	6	1.94 (4)	0.007 (3)	O	6	1.91 (1)	0.004 (4)	O	6	1.90
Me	6	2.87 (1)	0.013 (24)	Me	6	2.86 (1)	0.004 (3)	Co	6	2.85

[a] N was fixed during the fitting analysis. R (radial distance) and its uncertainty is marked with ΔR. The σ^2 (A^2) is the Debye-Waller factor. All parameters are reported with estimated uncertainties for the fitting exercises (provided in the parentheses in the table), except fixed parameters.

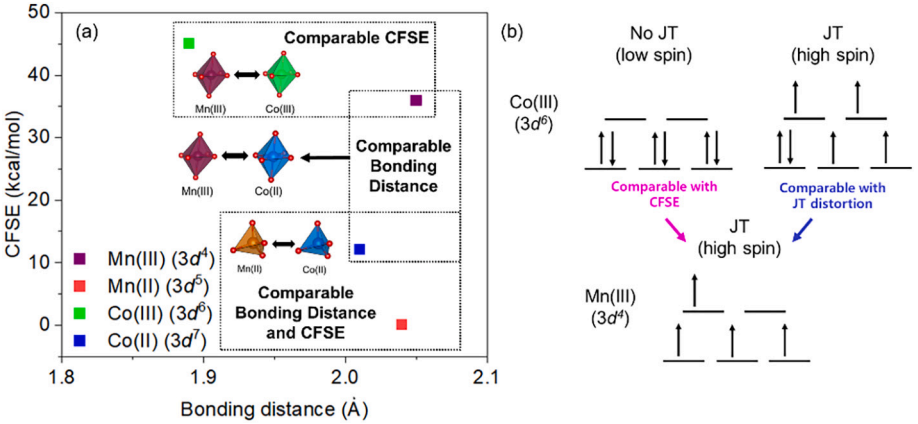

Fig. 8. Schematic diagrams of the likelihood in replacement between Mn and Co at tetrahedral or octahedral sites of hausmannite and manganite by (a) the CFSE and bonding distance values, and (b) the Jahn-Teller distortion impacted by Co(III) replacement at octahedral Mn(III) site of hausmannite.

The predominance of Co(II) in the manganite structure is in line with the study by McKenzie (1972), who concluded that Co(III) replacement with Mn(III) in the octahedral site of manganite is unlikely due to the small ionic radius. Since Co(II) in a LS configuration is of similar size to Mn(III) in manganite (Table S4), thus Co(II) would be a more feasible substituent, as evidenced by the longer bond distance of Co(II)-O demonstrated in our XAS analysis (McKenzie, 1972). This change in bond length may impact the stability of Co-substituted manganite toward the reductive dissolution reaction, leading it to behave differently than the pristine mineral phase. The combined consideration of bond lengths, CFSE effects, and the influence of the JT distorted Mn(III) can be useful for predicting the coordination chemistry of transition metal impurities in Mn(III) mineral structures (Fig. 8).

3.3.4. Co K-edge XANES of Co-substituted Mn(II/III) oxides after reductive dissolution

The reduction potential of Co(III/II) is larger than that of Mn(III/II) (Shannon, 1976), thus structural Co(III) may be involved in the oxidation of As(III) to As(V). As a result, reduced Co(II) may remain in the structure or be released to solution and then re-adsorbed on the mineral, where either pathway would result in a decrease of the average oxidation state (AOS) of post reaction material. To detect such changes, the Co *K*-edge XANES spectra of the mineral solids before and after the reductive dissolution were compared in SI Fig. S6. The results show that the absorption edge locations of the pre- and post-reacted phases are well-aligned, suggesting no change in the AOS of cobalt in Co2-Haus and Co2-Mang during reductive dissolution, although we do note a slight dampening of the edge height and near-edge oscillations, suggesting increased structural disorder in the reacted samples. In the case of manganite, the presence of redox-inactive Co(II) had little to no impact

on the oxidizing ability of the mineral toward As(III) oxidation (Fig. 3). The absence of changes in the oxidation state of solid-phase Co in reacted hausmannite may indicate that (i) structural Co(III) does not actively oxidize As(III) due to its trivial quantity; (ii) any reduced Co(II) is mostly released to solution; and/or (iii) the amount of structural or re-adsorbed Co(II) is comparably small relative to that of (unreacted) Co in the bulk mineral (SI Section 3.2.2, Table S6). Thus, the increased oxidizing ability of Co2-Haus (Fig. 2) may be attributed to accelerated mineral dissolution reactions, induced by the structural incorporation of Co, but not to Co(III) as a primary oxidizer of As(III).

3.3.5. *Mn K-edge XANES of pristine and Co-substituted Mn(II/III) oxides before and after reductive dissolution*

The Mn *K*-edge XANES spectra of pristine and Co-substituted Haus were identical, (Fig. 9(a)), indicating no major changes in Mn AOS resulting from Co substitution. In contrast, the Mn *K*-edge XANES spectrum of the Co2-Mang was notably different from that of the pristine Mang, indicating that Co substitution in the structure likely caused changes in the oxidation state and/or coordination environment of structural Mn (Fig. 9(b)). Among the changes, an increase in absorbance at higher energy in the absorption edge was observed, indicating the appearance of higher oxidation state Mn(IV) in Co2-Mang. To further examine the AOS of Mn in both minerals, and changes in the Mn AOS by Co substitution, LCF was performed on the XANES spectra using hausmannite (Mn(II/III)), manganite (Mn(III)), and birnessite (Mn(III/IV)) as reference materials. The results of LCF exercises yielded Mn AOS values of 2.70 and 3.14 in Co2-Haus and Co2-Mang, respectively. As the AOS of pristine manganite is 3, the increase in AOS of Mn in Co2-Mang further suggests the presence of Mn(IV) in the structure, which may be required to compensate for localized charge imbalance by Co(II) substituted at Mn(III) sites.

After the reductive dissolution with As(III), the absorption edge locations of pristine and Co-substituted Mn(II/III) oxides remained unchanged (Fig. S7), suggesting little to no change in Mn oxidation states in both minerals. A lack of change in Mn AOS was also noted in our previous study with Ni-substituted hausmannite minerals (Song et al., 2020). In addition, the results of PXRD analysis on As(III)-reacted minerals show essentially identical XRD patterns of both minerals before and after reductive dissolution (Fig. S8), in line with the XANES analysis. The absence of changes in Mn oxidation states of Co-substituted manganite after reductive dissolution with As(III) may also support our finding that Mn(IV) is not involved in the As(III) oxidation to As(V). The standard redox potential of Mn(IV) (i.e., MnO_2/Mn(II) = 1.23 eV) toward As(III) oxidation ($H_3AsO_3/HAsO_4^{2-}$ = −0.58 eV) is lower than that of Mn(III) in hausmannite (i.e., Mn_3O_4/Mn(II) = 1.50 eV) (Bratsch, 1989). Since Mn(II) is released into solution as a result of reductive dissolution no change in Mn AOS is expected.

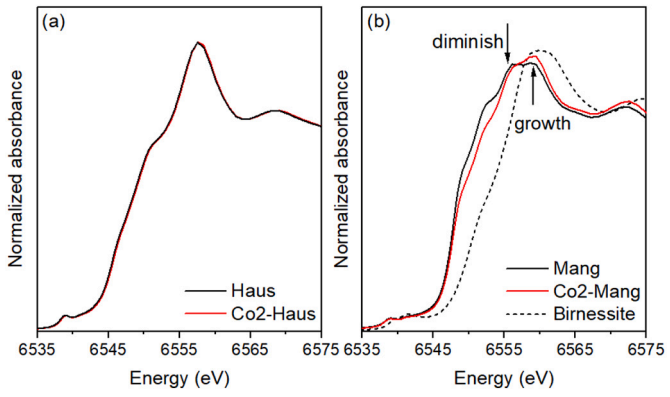

Fig. 9. Mn *K*-edge XANES in normalized absorbance (a) Haus and (b) Mang in the absence (black) and presence (red) of Co substitution (at a high substitution) with birnessite reference (dashed line), confirming the presence of Mn (IV). (For interpretation of the references to colour in this figure legend, the reader is referred to the web version of this article.)

3.4. *In-situ ATR-FTIR of pristine and Co-substituted Mn(II/III) oxides*

In-situ ATR-FTIR was used to identify the differences and complexities in coordination environments of As species on the mineral surfaces to compliment the EXAFS analyses. When the mineral surfaces were exposed to acidic dissolution conditions for 2 h (i.e., pH 5 in the absence of arsenite), no vibrational bands were observed suggesting that (1) acidic dissolution does not significantly alter the structure of the surface and (2) no formation of Mn hydroxide (946 cm^{-1}) or mineralogical conversion from hausmannite to manganite (1080–1150 cm^{-1}) were observed (Fig. S9A) (Elzinga, 2011). Due to small As(III/V) interactions with manganite, the in-situ ATR-FTIR results from manganite are presented in SI Fig. S9B and not discussed here.

When Haus was exposed to As(V), vibrational modes associated with the arsenate moiety grew in intensity and became distinctive from the baseline. In the spectrum of As(V)-reacted Haus, a growth of a broad band was noted between 900 and 700 cm^{-1} (Fig. 10(a)). While individual peak features were indistinguishable, this broad absorption can be generally defined as three vibrational modes of As(V) species, primarily the symmetric (ν_s) and antisymmetric (ν_{as}) As-O—stretches. These findings agree well with a study by Parikh et al. (2010) where three vibrational modes of As(V) complexes 908 cm^{-1} (antisymmetric (ν_{as}) stretch) and 875 cm^{-1} (symmetric (ν_s) stretch) of As-O— and 759–766 cm^{-1} ($\nu_s + \nu_{as}$ of As-OH—) on δ-MnO_2 surfaces were observed at pH 6. While it is difficult to identify each vibrational mode, an overall bathochromic shift, from the range of 908–759 cm^{-1} for modes of δ-MnO_2, was observed with As(V)-reacted Haus toward lower wavenumber (900–700 cm^{-1}) which can be attributed to the longer bond between As(V)-Mn(III) compared to shorter As(V)-Mn(IV) in δ-MnO_2. Furthermore, the broad intensity observed in the spectrum As(V)-reacted Haus suggests the presence of multiple complexations of As(V) on the hausmannite surface, consistent with the multiple peaks observed in the relative Fourier transform (Fig. S4(c)) and the shorter As(V)-O distance (Table S7) in the EXAFS analysis.

For the samples of As(III)-reacted pristine Haus and Co2-Haus, a continuous flow of an As(III) solution adjusted to pH 5 was run over a freshly made film of each mineral, while collecting spectra over the course of two hours. In both As(III)-reacted pristine Haus and Co2-Haus, an immediate growth of two vibrational modes was observed within the spectral regions that are indicative of As(V) interactions on the mineral surfaces. For instance, the As(III)-reacted pristine Haus displayed two vibration modes at 895 and 750 cm^{-1} (Fig. 10(b)), where the former corresponds to the ν_s and ν_{as} —As-O stretch, and the latter to the vibration associated with As(V)-O-Mn(III). However, the two modes were different in regard to overall peak intensities. The peak at 895 cm^{-1} was smaller and reached a maximum of the intensity after 60 min, whereas the peak at 750 cm^{-1} was higher in intensity and continued to grow over the full 2 h. This difference may indicate an early saturation of As(V) adsorption on or near the mineral surface (895 cm^{-1}), followed by a continuous formation of inner sphere As(V) complexes over the course of the reaction (750 cm^{-1}). In comparison to the As(V)-reacted Haus (Fig. 10(a)), the spectra of As(III)-reacted pristine Haus lacked a definite vibration located at 810 cm^{-1} that is associated with the oxidation of As (III) to As(V). The As(III) oxidation to As(V) is rapid and transient, and thus, detection of the vibration mode associated with this reaction is not feasible.

Similar to the As(III)-reacted Haus, the spectra of As(III)-reacted Co2-Haus showed (Fig. 10(c)) a peak at 895 cm^{-1}, assigned to (ν_s As-O— + ν_{as} —As-O), reaching a maxima at 60 min reaction time, and another at 750 cm^{-1}, growing in intensity throughout the reaction time, although the latter peak exhibited a slight shift toward lower wavenumber, 730 cm^{-1}, over the full two hours. The shift in peak maxima (750 to 730 cm^{-1}) found in the As(III)-reacted Co2-Haus was attributed

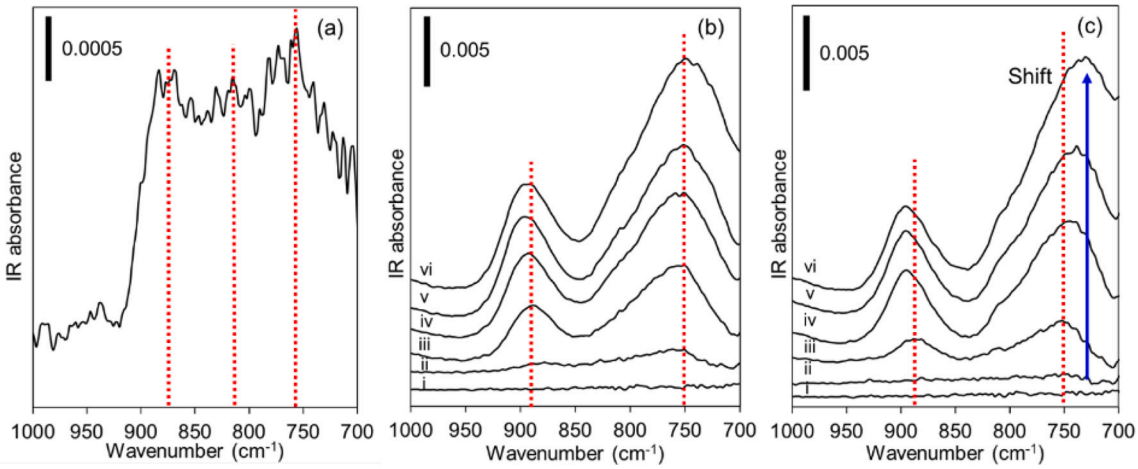

Fig. 10. Flow cell in-situ ATR-FTIR results: (a) As(V)-reacted Haus (measured in a static condition), (b) As(III)-reacted Haus, and (c) As(III)-reacted Co2-Haus in time sequence of (i) baseline, (ii) 0 (iii) 10, (iv) 30, (v) 60, and (vi) 120 min. The As(V)-O vibrational modes are marked with red dashed line. The blue arrow guides the peak growth ~705 cm^{-1} with Co2-Haus. Complementary figure is listed in SI (Fig. S10). (For interpretation of the references to colour in this figure legend, the reader is referred to the web version of this article.)

to the growth of vibrational band at 705 cm^{-1} (Fig. S10) identified by subtraction of subsequent spectra at the time of the peak shift. The new vibrational mode grew in for the remainder of the reaction time, and could be potentially assigned to multiple species, including As(III), a different As(V) complex, or a change in the Mn geometry. While not currently identifiable, the possibilities are intriguing and analysis could answer interesting questions about reactions at mineral surfaces. If the mode is attributable to As(III), it would suggest at early time points (within the initial 2 h analyzed here), As(III) builds up on the surface prior to converting fully to As(V) (the predominant species observed in XAS analysis after 8 h). Or if the mode is due to changes in Mn geometry as redox reactions occur, the analysis may yield an atomic level mechanism of As(III) oxidation at Mn surfaces. Future work is planned to elucidate the genesis of this vibration, which will help further determine complex environments of As species at mineral surfaces.

4. Conclusion

The present study investigates for the first time how, and to what extent, the structural incorporation of Co affects the stability and reactivity of hausmannite and manganite in a systematic manner. Hausmannite shows greater Co substitution effects than manganite, from changes in crystallographic and physicochemical properties to increases in both acidic and reductive dissolution reactions. Further, hausmannite exhibits enhanced oxidizing ability toward As(III), a property that also increased with Co substitution. While release of structural Co occurred during reductive dissolution of both sorbents, the majority of Co (more than 85% of initial Co) was found to remain in the mineral structures after reaction. Structural Co was found to contribute little as a primary oxidant of As(III).

The more pronounced effects of Co substitution in hausmannite than manganite can be explained by differences in the Co coordination geometry and oxidation states as probed by XAS analyses. The co-occupancy of Co(II) and Co(III) at tetrahedral and octahedral sites was identified in hausmannite, whereas in manganite only Co(II) substituted in octahedral sites was observed. The Co(II) occupancy in the manganite structure appears to impact the average Mn oxidation state in the mineral, with the formation of Mn(IV) observed in Co-substituted manganite, likely to compensate the charge imbalance induced by Co substitution. To interpret the observations, a theoretical analyses of CFSE and bond distances as well as JT distortion effects were used to explain the likelihood of Co substitutions in tetrahedral or octahedral sites of hausmannite and manganite, and Co(III) substitution in a LS configuration in hausmannite structure. Furthermore, we provide in-situ evidence of different coordination environments of As surface species induced by both the type of As species introduced and the presence of Co impurities in the mineral sorbent.

Thus, it is concluded that the coordination chemistry and valence of Co in the mineral structure has a significant impact on the stability and reactivity of the Mn(III)-containing oxide under dissolution conditions. Once incorporated in the mineral structure, Co solubility and mobility appear to be limited, even when the mineral undergoes dissolution reactions. Overall, this study successfully showcases that minerals with structural impurities exhibit geochemical behaviors that are different from their pristine equivalents. Therefore, careful examinations of the effects of metal impurities in minerals are required to gain a better understanding of natural Mn(II/III) oxides and their interactions with trace metals and metalloids in the environment.

Declaration of Competing Interest

The authors declare that they have no known competing financial interests or personal relationships that could have appeared to influence the work reported in this paper.

Acknowledgements

We acknowledge financial support from the National Science Foundation on the present study under Grant No. 2003866 and 2003364. We also thank the 6 BM and 7 BM beam scientists, Bruce Ravel (6 BM), and Syed Khalid and Steven Ehrlich (7 BM), for their support on XAS data acquisition and analysis. The present study used 6 BM and 7 BM beamlines of the National Synchrotron Light Source II, a U.S. Department of Energy (DOE) Office of Science User Facility operated for the DOE Office of Science by Brookhaven National Laboratory under Contract No. DE-SC0012704. The authors also thank to Dr. Fan Liu (Huazhong Agricultural University, China) for providing the XAS spectrum for CoOOH. Boyoung Song also appreciates the Clay Minerals Society for the Research Grant Award to support a part of this study.

Appendix A. Supplementary data

Supplementary data to this article can be found online at https://doi.org/10.1016/j.chemgeo.2021.120453.

References

Barreto, M.S.C., Elzinga, E.J., Alleoni, L.R.F., 2020. Hausmannite as potential As(V) filter. Macroscopic and spectroscopic study of As(V) adsorption and desorption by citric acid. Environ. Pollut. 262, 114196.

Bhandari, N., Hausner, D.B., Kubicki, J.D., Strongin, D.R., 2010. Photodissolution of ferrihydrite in the presence of oxalic acid: an in situ ATR-FTIR/DFT study. Langmuir 26, 16246–16253.

Bratsch, S.G., 1989. Standard electrode potentials and temperature coefficiencts in water at 298.15 K. J. Phys. Chem. Ref. Data 18, 1–21.

Burns, R.G., 1976. The uptake of cobalt into ferromanganese nodules, soils, and synthetic manganese (IV) oxides. Geochim. Cosmochim. Acta 40, 95–102.

Burns, R.G., Burns, V.M., Easton, A.J., 1977. The mineralogy and crystal chemistry of deep-sea manganese nodules, a polymetallic resource of the twenty-first century. Philos. Trans. R. Soc. London. Ser. A 286, 283–301.

Carpenter, R.H., Robinson, G.D., Hayes, W.B., 1978. Partitioning of manganese, iron, copper, zinc, lead, cobalt, and nickel in black coatings on stream boulders in the vicinity of the Magruder mine, Lincoln Co., Georgia. J. Geochem. Explor. 10, 75–89.

Cerkez, E.B., Bhandari, N., Reeder, R.J., Strongin, D.R., 2015. Coupled redox transformation of chromate and arsenite on ferrihydrite. Environ. Sci. Technol. 49, 2858–2866.

Chiu, V.Q., Hering, J.G., 2000. Arsenic adsorption and oxidation at manganite surfaces. 1. Method for simultaneous of determination of adsorbed and dissolved arsenic species. Environ. Sci. Technol. 2029–2034.

Crowther, D.L., Dillard, J.G., Murray, J.W., 1983. The mechanisms of Co(II) oxidation on synthetic birnessite. Geochim. Cosmochim. Acta 47, 1399–1403.

Dillard, J.G., Crowther, D.L., Murray, J.W., 1982. The oxidation states of cobalt and selected metals in Pacific ferromanganese nodules. Geochim. Cosmochim. Acta 46, 755–759.

Eitel, E.M., Zhao, S., Tang, Y., Taillefert, M., 2018. Effect of manganese oxide aging and structure transformation on the kinetics of thiol oxidation. Environ. Sci. Technol. 52, 13202–13211.

Elzinga, E.J., 2011. Reductive transformation of birnessite by aqueous Mn(II). Environ. Sci. Technol. 45, 6366–6372.

Goldberg, E.D., 1954. Marine geochemistry 1. Chemical scavengers of the sea. J. Geol. 62, 249–265.

Green, W.J., Stage, B.R., Bratina, B.J., Wagers, S., Preston, A., O'Bryan, K., Shacat, J., Newell, S., 2004. Nickel, copper, zinc and cadmium cycling with manganese in Lake Vanda (Wright Valley, Antarctica). Aquat. Geochem. 10, 303–323.

Guo, S., Sun, W., Yang, W., Li, Q., Shang, J.K., 2015. Superior As(III) removal performance of hydrous MnOOH nanorods from water. RSC Adv. 5, 53280–53288.

Hein, J.R., Koschinsky, A., 2014. Deep-ocean ferromanganese crusts and nodules. Treatise Geochem. 273–291.

Hem, J.D., 1978. Redox processes at surfaces of manganese oxide and their effects on aqueous metal ions. Chem. Geol. 21, 199–218.

Hem, J.D., Lind, C.J., 1994. Chemistry of manganese precipitation in Pinal Creek, Arizona, USA: a laboratory study. Geochim. Cosmochim. Acta 58, 1601–1613.

Hem, J.D., Lind, C.J., Roberson, C.E., 1989. Coprecipitation and redox reactions of manganese oxides with copper and nickel. Geochim. Cosmochim. Acta 53, 2811–2822.

Hens, T., Brugger, J., Cumberland, S.A., Etschmann, B., Frierdich, A.J., 2018. Recrystallization of manganite (γ-MnOOH) and implications for trace element cycling. Environ. Sci. Technol. 52, 1311–1319.

Hu, C.C., Wu, Y.T., Change, K.H., 2008. Low-temperature hydrothermal synthesis of Mn_3O_4 and MnOOH single crystals: determinant influence of oxidants. Chem. Mater. 2890–2894.

Junta, J.L., Hochella, M.F., 1994. Manganese(II) oxidation at mineral surfaces: a microscopic and spectroscopic study. Geochim. Cosmochim. Acta 58, 4985–4999.

Kay, J.T., Conklin, M.H., 2001. Processes of nickel and cobalt uptake by a manganese oxide forming sediment in Pinal Creek, Globe mining district, Aerizona. Environ. Sci. Technol. 35, 4719–4725.

Koschinsky, A., Halbach, P., 1995. Sequential leaching of marine ferromanganese precipitates: genetic implications. Geochim. Cosmochim. Acta 59, 5113–5132.

Lee, Y., Tebo, B.M., 1994. Cobalt(II) oxidation by the marine manganese(II)-oxidizing Bacillus sp. Strain SG-1. Appl. Environ. Microbiol. 60, 2949–2957.

Luo, Y., Li, S., Tan, W., Qiu, G., Liu, F., Cai, C., 2017. Oxidation and catalytic oxidation of dissolved sulfide by manganite in aqueous systems. Clay Clay Miner. 65, 299–309.

Luo, Y., Tan, W., Suib, S.L., Qiu, G., Liu, F., 2018. Dissolution and phase transformation processes of hausmannite in acidic aqueous systems under anoxic conditions. Chem. Geol. 487, 54–62.

Manceau, A., Llorca, S., Calas, G., 1987. Crystal chemistry of cobalt and nickel in lithiophorite and asbolane from New Caledonia. Geochim. Cosmochim. Acta 51, 105–113.

Manceau, A., Gorshkov, A.I., Drits, V.A., 1992. Structural chemistry of Mn, Fe, Co, and Ni in manganese hydrous oxides: Part II. Information from EXAFS spectroscopy and electron and X-ray diffraction. Am. Mineral. 77, 1144–1157.

Manceau, A., Drits, V.A., Silvester, E., Bartoli, C., Lanson, B., 1997. Structural mechanism of Co^{2+} oxidation by the phyllomanganate buserite. Am. Mineral. 82, 1150–1175.

McClure, D.S., 1957. The distribution of transition metal cations in spinels. J. Phys. Chem. Solids 3, 311–317.

McKenzie, R.M., 1971. The synthesis of birnessite, cryptomelane, and some other oxides and hydroxides of manganese. Mineral. Mag. 38, 493–502.

McKenzie, R.M., 1972. The sorption of some heavy metals by the lower oxides of manganese. Geoderma 8, 29–35.

Miyasaka, T., Kurokawa, A., Takeuchi, H., Yano, S., Yanoh, T., Onuma, K., Kondo, T., Miike, K., Ichiyanagi, Y., 2012. Magnetic properties and X-ray absorption fine-structure spectra of $CoMn_2O_4$ nanoparticles. J. Surf. Sci. Nanotechnol. 10, 643–646.

Murray, J.W., Dillard, J.G., 1979. The oxidation of cobalt(II) adsorbed on manganese dioxide. Geochim. Cosmochim. Acta 43, 781–787.

Murray, J.W., Dillard, J.G., Giovanoli, R., Moers, H., Stumm, W., 1985. Oxidation of Mn (II): initial mineralogy, oxidation state and ageing. Geochim. Cosmochim. Acta 49, 463–470.

Nesbitt, H.W., Canning, G.W., Bancroft, G.M., 1998. XPS study of reductive dissolution of 7Å-birnessite by H_3AsO_3, with constraints on reaction mechanism. Geochim. Cosmochim. Acta 62, 2097–2110.

Ostwald, J., 1984. Two varieties of lithiophorite in some Australian deposits. Mineral. Mag. 48, 383–388.

Parikh, S.J., Lafferty, B.J., Meade, T.G., Sparks, D.L., 2010. Evaluating environmental influences on As^{III} oxidation kinetics by a poorly crystalline Mn-oxide. Environ. Sci. Technol. 44, 3772–3778.

Peña, J., Duckworth, O.W., Bargar, J.R., Sposito, G., 2007. Dissolution of hausmannite (Mn_3O_4) in the presence of the trihydroxamate siderophore desferrioxamine B. Geochim. Cosmochim. Acta 71, 5661–5671.

Ramstedt, M., Andersson, B.M., Shchukarev, A., Sjöberg, S., 2004. Surface properties of hydrous manganite (γ-MnOOH). A potentiometric, electroacoustic, and X-ray photoelectror spectroscopy study. Langmuir 20, 8224–8229.

Ravel, B., Newville, M., 2005. ATHENA, ARTEMIS, HEPHAESTUS: data analysis for X-ray absorption spectroscopy using IFEFFIT. J. Synchrotron Radiat. 12, 537–541.

Shacat, J.A., Green, W.J., Decarlo, E.H., Newell, S., 2004. The geochemistry of Lake Joyce, McMurdo Dry Valleys, Antarctica. Aquat. Geochem. 10, 325–352.

Shannon, R.D., 1976. Revised effective ionic radii and systematic studies of interatomie distances in halides and chaleogenides. Acta Cryst A32, 751–767.

Shaughnessy, D.A., Nitsche, H., Booth, C.H., Shuh, D.K., Waychunas, G.A., Wilson, R.E., Gill, H., Cantrell, K.J., Serne, R.J., 2003. Molecular interfacial reactions between Pu (VI) and manganese oxide minerals manganite and hausmannite. Environ. Sci. Technol. 37, 3367–3374.

Silva, G.C., Almeida, F.S., Dantas, M.S.S., Ferreira, A.M., Ciminelli, V.S.T., 2013. Raman and IR spectroscopic investigation of As adsorbed on Mn_3O_4 magnetic composites. Spectrochim. Acta - Part A Mol. Biomol. Spectrosc. 100, 161–165.

Silvester, E., Manceau, A., 1997. The structure of synthetic monoclinic Na-rich birnessite and hexagonal birnessite: II. Results from chemical studies and EXAFS spectroscopy. Am. Mineral. 82, 946–961.

Simanova, A.A., Peña, J., 2015. Time-resolved investigation of cobalt oxidation by Mn (III)-rich δ-MnO_2 using quick X-ray absorption spectroscopy. Environ. Sci. Technol. 49, 10867–10876.

Song, B., Cerkez, E.B., Elzinga, E.J., Kim, B., 2020. Effects of Ni incorporation on the reactivity and stability of hausmannite (Mn_3O_4): environmental implications for Mn, Ni, and As solubility and cycling. Chem. Geol. 558, 119862.

Song, B., Cerkez, E.B., Grandstaff, D.E., Goodwin, C.M., Beebe, T.P., Kim, B., 2021. Reactivity of binary manganese oxide mixtures towards arsenite removal: evidence of synergistic effects. Appl. Geochem. 104939.

Song, R., Wang, H.-J., Shou-Hua, F., 2012. Solvothermal preparation of Mn_3O_4 nanoparticles and effect of temperature on particle size. Chem. Res. Chin. Univ. 28, 577–580.

Stumm, W., Giovanoli, R., 1976. On the nature of particulate manganese in simulated lake waters. Chimia (Aarau). 30, 423–425.

Suchow, L., 1976. A detailed, simple crystal field consideration of the normal spinel structure of Co_3O_4. J. Chem. Educ. 53, 560.

Tan, H., Zhang, G., Heaney, P.J., Webb, S.M., Burgos, W.D., 2010. Characterization of manganese oxide precipitates from Appalachian coal mine drainage treatment systems. Appl. Geochem. 25, 389–399.

Taylor, R.M., 1968. The association of manganese and cobalt in soils - further observations. J. Soil Sci. 19, 77–80.

Taylor, R.M., McKenzie, R.M., 1966. The association of trace elements with manganese minerals in Australian soils. Soil Res. 4, 29–39.

Taylor, R.M., McKenzie, R.M., Norrish, K., 1964. The mineralogy and chemistry of manganese in some Australian soils. Soil Res. 2, 235–248.

U.S. EPA, 2007. "Method 3051A (SW-846): Microwave Assisted Acid Digestion of Sediments, Sludges, and Oils", Revision 1 (Washington, D.C.).

Vodyanitskii, Y.N., 2009. Mineralogy and geochemistry of manganese: a review of publications. Eurasian Soil Sci. 42, 1170–1178.

Weaver, R.M., Hochella, M.F., 2003. The reactivity of seven Mn-oxides with $Cr^{3+}_{(aq)}$: a comparative analysis of a complex, aqueous environmentally important redox reaction. Am. Mineral. 88, 2016–2027.

Weaver, R.M., Hochella, M.F., Ilton, E.S., 2002. Dynamic processes occurring at the Cr $(III)_{aq}$-manganite (γ-MnOOH) interface: simultaneous adsorption, microprecipitation, oxidation/reduction, and dissolution. Geochim. Cosmochim. Acta 66, 4119–4132.

Wilk, P.A., Shaughnessy, D.A., Wilson, R.E., Nitsche, H., 2005. Interfacial interactions between Np(V) and manganese oxide minerals manganite and hausmannite. Environ. Sci. Technol. 39, 2608–2615.

Wright, P.A., Natarajan, S., Thomas, J.M., Gai-Boyes, P.L., 1992. Mixed-metal amorphous and spinel phase oxidation catalysts: characterization by X-ray diffraction, X-ray absorption, electron microscopy, and catalytic studies of systems containing copper, cobalt, and manganese. Chem. Mater. 4, 1053–1065.

Wu, Z., Peacock, C.L., Lanson, B., Yin, H., Zheng, L., Chen, Z., Tan, W., Qiu, G., Liu, F., Feng, X., 2019. Transformation of Co-containing birnessite to todorokite: effect of Co on the transformation and implications for Co mobility. Geochim. Cosmochim. Acta 246, 21–40.

Yamamoto, N., Kawano, S., Achiwa, N., Higashi, S., 1983. Preparation by a wet method and ionic distribution of transition metal-substituted hausmannite spinel. J. Jpn. Metal. Soc. 30, 48–54.
Yildirim, B., Riesen, H., 2013. Coordination and oxidation state analysis of cobalt in nanocrystalline $LiGa_5O_8$ by X-ray absorption spectroscopy coordination and oxidation state analysis of cobalt in nanocrystalline. J. Phys. Conf. Ser. 430, 1–5.
Yin, H., Feng, X., Qiu, G., Tan, W., Liu, F., 2011. Characterization of Co-doped birnessites and application for removal of lead and arsenite. J. Hazard. Mater. 188, 341–349.
Yin, H., Li, H., Wang, Y., Ginder-Vogel, M., Qiu, G., Feng, X., Zheng, L., Liu, F., 2014. Effects of Co and Ni co-doping on the structure and reactivity of hexagonal birnessite. Chem. Geol. 381, 10–20.
Yu, Q., Sasaki, K., Tanaka, K., Ohnuki, T., Hirajima, T., 2012. Structural factors of biogenic birnessite produced by fungus Paraconiothyrium sp. WL-2 strain affecting sorption of Co^{2+}. Chem. Geol. 310–311, 106–113.